

See discussions, stats, and author profiles for this publication at: <https://www.researchgate.net/publication/256463319>

Syntheses, Structural, Computational and Thermal Analysis of Acid–Base Complexes of Picric Acid with N–Heterocyclic Bases

ARTICLE in THE JOURNAL OF PHYSICAL CHEMISTRY A · SEPTEMBER 2013

Impact Factor: 2.69

READS

76

2 AUTHORS:



Nidhi Goel

Indian Institute of Science

24 PUBLICATIONS 191 CITATIONS

SEE PROFILE



Udai P Singh

University of South Carolina

108 PUBLICATIONS 1,784 CITATIONS

SEE PROFILE

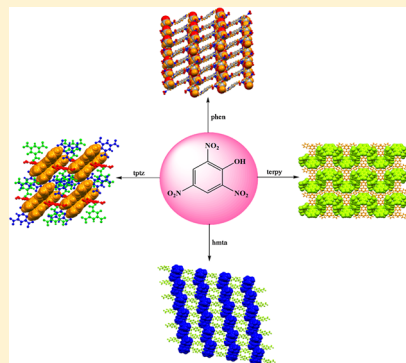
Syntheses, Structural, Computational, and Thermal Analysis of Acid–Base Complexes of Picric Acid with N-Heterocyclic Bases

Nidhi Goel* and Udai P. Singh

Department of Chemistry, Indian Institute of Technology Roorkee, Roorkee 247 667, India

S Supporting Information

ABSTRACT: Four new acid–base complexes using picric acid $[(\text{OH})(\text{NO}_2)_3\text{C}_6\text{H}_2]$ (PA) and N-heterocyclic bases (1,10-phenanthroline (phen)/2,2',6',2''-terpyridine (terpy)/hexamethylenetetramine (hmta)/2,4,6-tri(2-pyridyl)-1,3,5-triazine (tptz)) were prepared and characterized by elemental analysis, IR, NMR and X-ray crystallography. Crystal structures provide detailed information of the noncovalent interactions present in different complexes. The optimized structures of the complexes were calculated in terms of the density functional theory. The thermolysis of these complexes was investigated by TG-DSC and ignition delay measurements. The model-free isoconversional and model-fitting kinetic approaches have been applied to isothermal TG data for kinetics investigation of thermal decomposition of these complexes.



1. INTRODUCTION

The strategy for creating new acid–base complexes^{1–4} is usually based on strong directional hydrogen bonding, as hydrogen bonding is the main driving force in construction of supramolecular solids.^{5–12} It is well-known that these complexes represent a new class of compounds due to their different properties than the individual acid and bases as well. These have received much attention over the past several years because of their potential applications as functional materials.^{13,14} Picric acid with three nitro groups forms crystalline picrates with various organic molecules through ionic, non-covalent, and π – π interactions as these interactions have been widely utilized as a supramolecular heterosynthon in the design of new complexes.^{15,16} It is known that picric acid acts not only as an acceptor but also as an acidic ligand, and has strong tendency to form the hydrogen bonds with N-heterocyclic bases.¹⁷ Instead of these characteristics, picric acid is used to produce very sensitive compounds because the nitro groups are the powerful oxidizing groups, which decompose and explode at elevated temperature. N-heterocyclic bases are chosen as one of the secondary components because they participate in hydrogen bonding with picric acid, and have a higher heat of formation, density, and oxygen balance than the carbocyclic analogues. Due to these attractive features, picric acid and N-heterocyclic bases are used for the preparation of acid–base complexes. In the past, a large number of acid–base complexes having heterocyclic bases have been studied^{18–25} but the mechanism of thermal analysis and ignition delay measurement are not reported for these systems in literature. Here, we report the synthesis, structural characterization, and thermal analysis of newly constructed complexes of picric acid with N-heterocyclic bases (phen, terpy, hmta, tptz), and also the effect of the increasing nitrogen content in the secondary organic

moieties on the supramolecular network, thermolysis, and kinetic behavior of picric acid.

2. EXPERIMENTAL SECTION

All manipulations were performed in air using commercial grade solvents. Picric acid (2,4,6-trinitrophenol), 1,10-phenanthroline (phen)/2,2',6',2''-terpyridine (terpy)/hexamethylenetetramine (hmta)/2,4,6-tri(2-pyridyl)-1,3,5-triazine (tptz) were purchased from Aldrich Chemical Co. (St. Louis, MO, USA).

2.1. Synthesis of Complexes 1–4. The complexes 1–4, were synthesized by the stoichiometric combination of picric acid and N-heterocyclic bases (phen/terpy/hmta/tptz) as shown in Scheme 1.

[PA[−]·phenH⁺·CH₃OH] (1). Picric acid (0.22 g, 1.0 mmol) and phen (0.19 g, 1.0 mmol) were mixed in an acetonitrile-methanol mixture (v/v %, 1:4, 10 mL). The resulting solution was stirred for 6 h and filtered through Celite. The filtrate was evaporated until dryness under vacuum, and the yellow solid obtained was redissolved in methanol. The yellow crystals of 1 in 62.5% (0.27 g, 0.62 mmol) yield, suitable for X-ray data collection were obtained by slow evaporation of solvent at room temperature. Anal. Calcd (%) for C₁₉H₁₅N₅O₈ (441.36): C, 51.71; H, 3.42; N, 15.86. Found: C, 51.59; H, 3.33; N, 15.73. IR (KBr, cm^{−1}): 3357, 3056, 1514, 1364, 1312, 1263, 1159, 1076, 1016, 909, 847, 785, 744, 715, 619. ¹H NMR (DMSO-*d*₆, ppm), δ : 8.74 (s, 2H, PA[−]), 7.43 (d, 1H, CH), 7.93 (dd, 1H, CH), 8.11 (d, 1H, CH), 8.27 (d, 1H, CH), 8.81 (dd, 1H, CH), 9.23 (d, 1H, CH), 9.67 (d, 1H, CH), 9.84 (d, 1H, CH), 12.09 (s, br, 1H, NH), 3.15 (s, 3H, OCH₃).

Received: June 2, 2013

Revised: August 13, 2013

Scheme 1. General Method for Preparation of Complexes 1-4

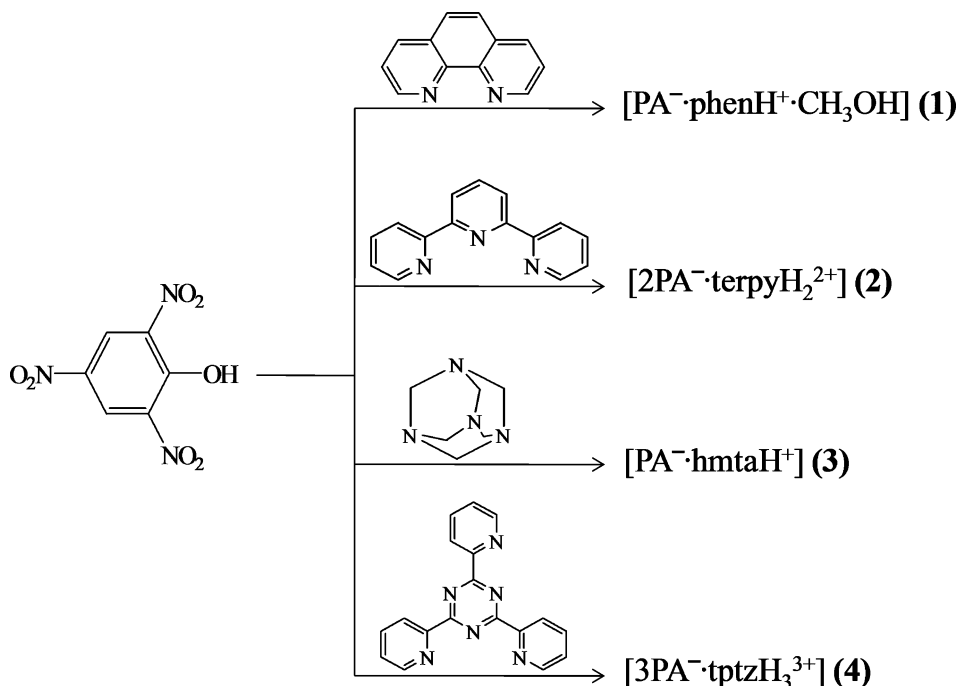


Table 1. Crystallographic Data and Structure Refinement Parameters for 1-4

complexes	1	2	3	4
formula	C ₁₉ H ₁₅ N ₅ O ₈	C ₂₇ H ₁₇ N ₉ O ₁₄	C ₁₂ H ₁₅ N ₇ O ₇	C ₃₆ H ₂₁ N ₁₅ O ₂₁
formula weight	441.36	691.50	369.31	999.68
temprature	296(2)	296(2)	296(2)	296(2)
crystal system	triclinic	monoclinic	monoclinic	triclinic
space group	P $\bar{1}$	P2 ₁ /c	P2 ₁ /c	P $\bar{1}$
<i>a</i> (Å)	9.874(3)	16.8357(12)	12.4862(5)	12.0003(12)
<i>b</i> (Å)	10.102(2)	22.0386(16)	6.5794(2)	12.4492(12)
<i>c</i> (Å)	10.903(3)	7.6284(5)	18.5303(7)	14.3966(14)
α (deg)	67.235(13)	90.00	90.00	70.367(5)
β (deg)	71.296(13)	95.850(3)	107.044(2)	87.593(5)
γ (deg)	82.679(14)	90.00	90.00	73.857(5)
<i>V</i> (Å ³)	949.8(4)	2815.7(3)	1455.44(9)	1942.7(3)
<i>Z</i>	2	4	4	2
<i>D</i> _{calc} (g/cm ³)	1.543	1.631	1.685	1.709
μ (Mo K α) (cm ⁻¹)	0.123	0.135	0.141	0.145
<i>F</i> (000)	456	1416	768	1020
crystal size	0.24 × 0.19 × 0.11	0.31 × 0.26 × 0.22	0.24 × 0.19 × 0.14	0.31 × 0.27 × 0.21
θ range for data collection (deg)	2.19–30.89	3.03–25.0	1.71–28.91	1.50–28.57
no. of measured reflections	5856	4950	3778	9852
no. of observed reflections	3119	3533	2973	7789
no. of data/restraints/parameters	5856/0/295	4950/0/459	3778/0/239	9852/0/661
goodness-of-fit	0.670	0.814	0.847	1.076
final R indices [<i>I</i> > 2(<i>I</i>)]				
<i>R</i> ₁ ^a	0.0497	0.0813	0.0382	0.0496
<i>wR</i> ₂ ^b	0.1303	0.2161	0.1109	0.1438

$$^a R_1 = \sum ||F_o| - |F_c|| / \sum |F_o|, \quad ^b wR_2 = \{ \sum [w(F_o^2 - F_c^2)]^2 / \sum w(F_o^2)^2 \}^{1/2}.$$

[2PA⁻·terpyH₂²⁺] (2). Complex 2 was prepared by the same procedure as outlined above for 1 using terpy (0.23 g, 1.0 mmol) with 72.8% (0.50 g, 0.72 mmol) yield. Anal. Calcd (%) for C₂₇H₁₇N₉O₁₄ (691.50): C, 46.90; H, 2.47; N, 18.23. Found: C, 46.78; H, 2.38; N, 18.11. IR (KBr, cm⁻¹): 3429, 3098, 1860, 1635, 1527, 1435, 1337, 1269, 1160, 1080, 915, 834, 780, 704. ¹H NMR (DMSO-*d*₆, ppm), δ : 8.75 (s, 2H, PA⁻), 7.89 (d, 2H,

CH), 8.19 (t, 1H, CH), 8.31 (t, 2H, CH), 8.97 (t, 2H, CH), 9.45 (d, 2H, CH), 9.87 (d, 2H, CH), 12.39 (s, br, 2H, NH).

[PA⁻·hmtaH⁺] (3). The same procedure was applied on complex 3 as outlined above for 1 using hmta (0.14 g, 1.0 mmol) with 73.7% (0.27 g, 0.73 mmol) yield. Anal. Calcd (%) for C₁₂H₁₅N₇O₇ (369.31): C, 39.03; H, 4.09; N, 26.55. Found: C, 38.91; H, 3.98; N, 26.42. IR (KBr, cm⁻¹): 3438, 2917, 2552,

1629, 1562, 1483, 1433, 1404, 1361, 1287, 1257, 1156, 1014, 978, 820, 791, 708. ^1H NMR ($\text{DMSO}-d_6$, ppm), δ : 8.74 (s, 2H, PA^-), 3.83 (s, 4H, CH_2), 4.78 (s, 8H, CH_2), 12.21 (s, br, 1H, NH).

$[3\text{PA}^-\text{tptzH}_3^{3+}]$ (4). Complex 4 was also prepared by the same procedure as outlined above for 1 using tptz (0.31 g, 1.0 mmol) with 68.9% (0.68 g, 0.68 mmol) yield. Anal. Calcd (%) for $\text{C}_{36}\text{H}_{21}\text{N}_{15}\text{O}_{21}$ (999.68): C, 43.25; H, 2.11; N, 21.01. Found: C, 43.12; H, 2.05; N, 20.91. IR (KBr, cm^{-1}): 3426, 3104, 1860, 1633, 1609, 1531, 1434, 1342, 1272, 1155, 1087, 918, 830, 778, 732, 705, 660. ^1H NMR ($\text{DMSO}-d_6$, ppm), δ : 8.76 (s, 2H, PA^-), 8.81 (t, 3H, CH), 9.01 (d, 3H, CH), 9.52 (t, 3H, CH), 9.87 (d, 3H, CH), 12.49 (s, br, 3H, NH).

2.2. Instrumentation. Elemental Analysis, Infrared, and NMR Spectroscopy. Crystallized complexes were carefully dried under vacuum for several hours prior to elemental analysis on Elementar Vario EL III analyzer. IR spectra were obtained on a Thermo Nicolet Nexus FT-IR spectrometer in KBr. ^1H NMR spectra were recorded on Bruker-D-Avance 500 MHz spectrometer with Fourier transform technique using tetramethylsilane as internal standard.

X-ray Diffraction Data. The X-ray data collection were performed on a Bruker Kappa Apex four circle-CCD diffractometer using graphite monochromated Mo $K\alpha$ radiation ($\lambda = 0.71070 \text{ \AA}$) at 100 K. In the reduction of data Lorentz and polarization corrections, empirical absorption corrections were applied.²⁶ Crystal structures were solved by direct methods. Structure solution, refinement, and data output were carried out with the SHELXTL program.^{27,28} Non-hydrogen atoms were refined anisotropically. Hydrogen atoms were placed in geometrically calculated positions by using a riding model. Images and hydrogen bonding interactions were created in the crystal lattice with DIAMOND and MERCURY softwares.^{29,30} The crystallographic data and the selected hydrogen bond distances are given in Tables 1 and 2, respectively.

2.3. Computational and Statistical Analysis. The geometry optimization of the different complexes have been performed by density functional theory (DFT) with a hybrid function B3LYP at the 6-31G** basis set by the Gaussian 03 program.^{31–33} The coordinates for performing the theoretical calculations were given in the form of the z-matrix generated by GaussView. ChemCraft1.5 and GaussView were used for the visualization of the output file and comparing the simulated data with the experimental crystallographic one. The experimental and simulated values for bond length and bond angles were statistically tested for significance in MATLAB R2008a toolbox. The *t* test was performed to analyze the data, and the *p*-value was calculated between experimental and simulated data, which is used to measure the potency and direction of a linear association between two variables. In statistical hypothesis, the *p*-value is the probability of obtaining a test statistic at least as extreme as the one that was actually observed, assuming that the null hypothesis is true. One often rejects the null hypothesis, when the *p*-value is less than the predetermined significance level, which is often 0.05 or 0.01, representing observed result would be highly unlikely under the null hypothesis.

2.4. Thermal Analysis. Thermogravimetry and differential scanning calorimetry (TG-DSC) were carried out at $10^\circ\text{C}/\text{min}$ (mass 0.055 g) under a nitrogen atmosphere at the flow rate of 200 mL/min on Perkin Elmer's (Pyris Diamond) (Woodland, California, USA) thermogravimetric analyzer, and the isothermal TG studies (mass 0.033 g, 100–200 mesh) of 1–4

Table 2. Noncovalent Interactions for 1–4 (\AA and deg)

D–H...A	<i>d</i> (D–H)	<i>d</i> (H–A)	<i>d</i> (D–A)	\angle (DHA)
[$\text{PA}^-\text{phenH}^+\text{CH}_3\text{OH}$] (1)				
O8–H8...O1	0.820	2.002(3)	2.2767	155.1
O8–H8...O4	0.820	2.419(19)	2.993	127.8
N1–H1B...O8	0.896	1.831 (29)	2.682	157.7
C7–H7A...O1	0.930	2.338(18)	3.218	157.7
C7–H7A...O2	0.930	2.404(9)	3.114	133.0
C9–H9...O3	0.930	3.016(19)	3.757	137.7
C11–H11...O3	0.930	2.628(9)	3.457	148.8
C12–H12...O6	0.930	2.840(21)	3.741	163.5
C14–H14...O7	0.930	2.41(2)	3.300	160.3
C15–H15...O8	0.930	2.839(5)	3.340	115.0
C16–H16...O8	0.929	2.807(4)	3.338	117.4
C19–H19C...O3	0.930	2.746(7)	3.620	151.5
[$2\text{PA}^-\text{terpyH}_2^{2+}$] (2)				
N1–H1A...O8	0.964	2.031(110)	2.718	126.6
N3–H3A...O8	0.997	1.727(49)	2.694	162.4
C4–H4...O12	0.929	2.697(3)	3.595	162.7
C7–H7...O11	0.931	2.714(3)	3.450	136.6
C7–H7...O12	0.931	2.619(3)	3.524	164.3
C8–H8...O5	0.930	2.949(8)	3.618	130.1
C9–H9...O1	0.930	2.287(5)	3.178	160.2
C12–H12...O1	0.930	2.380(4)	3.305	172.9
C13–H13...O2	0.930	2.489(8)	3.098	123.2
C13–H13...O11	0.930	2.600(3)	3.361	139.3
C14–H14...O5	0.929	2.121(7)	3.707	143.2
C15–H15...O4	0.930	2.328(7)	3.147	146.7
[$\text{PA}^-\text{hmtaH}^+$] (3)				
N6–H6...O1	0.863	1.864(25)	2.664	153.2
C3–H3...O2	0.930	2.958(2)	3.064	127.5
C7–H7B...O5	0.970	2.925(2)	3.870	165.1
C8–H8B...O4	0.969	2.804(4)	3.733	160.6
C9–H9B...O1	0.969	2.987(1)	3.190	93.08
C9–H9B...O3	0.969	2.918(2)	3.208	98.58
C9–H9B...O6	0.969	2.707(1)	3.326	145.3
C9–H9B...O7	0.969	3.017(2)	3.511	141.0
C11–H11B...O3	0.969	2.590(2)	3.239	124.4
C12–H12A...O4	0.970	2.401(1)	3.351	166.1
C7–H7A...N7	0.970	2.800(2)	3.662	148.4
C8–H8A...N5	0.970	2.852(1)	3.393	116.1
C8–H8B...N4	0.969	2.817(1)	3.460	124.5
C8–H8B...N5	0.969	3.074(2)	3.393	117.8
C10–H10B...N7	0.971	2.801(3)	3.662	148.2
C11–H11B...N4	0.969	2.724(2)	3.387	126.1
C12–H12A...N7	0.970	3.071(1)	3.379	110.1
C12–H12B...N7	0.969	2.908(3)	3.379	111.0
[$3\text{PA}^-\text{tptzH}_3^{3+}$] (4)				
N10–H10...O17	0.831	2.637(24)	3.084	115.1
N12–H12A...O8	0.867	1.931(26)	2.791	170.3
N15–H15...O20	1.102	2.243(29)	3.262	152.7
N15–H15...O21	1.102	2.777(29)	3.590	130.3
C19–H19...O14	0.931	2.484(5)	3.327	150.6
C19–H19...O17	0.931	2.795(8)	3.197	107.2
C20–H20...O17	0.930	2.633(5)	3.175	117.8
C21–H21...O18	0.930	2.661(2)	3.540	157.9
C22–H22...O20	0.930	2.839(8)	3.608	140.7
C28–H28...O15	0.930	2.649(6)	3.238	121.8
C28–H28...O16	0.930	2.534(6)	3.454	169.5
C29–H29...O15	0.930	2.601(6)	3.217	124.1
C33–H33...O8	0.929	1.955(4)	2.872	168.4

were also performed at appropriate temperatures (290–330 °C) in static air using an indigenously fabricated TG apparatus³⁴ fitted with temperature cum controller. The ignition delay (D_i) data were recorded using tube furnace technique³⁵ (mass 0.020 g, 100–200 mesh) in the temperature range 380–420 °C (± 1 °C). Each run was repeated five times and the mean D_i values were calculated. The D_i data were found to fit in the following equation^{36–38}

$$D_i = Ae^{E_a^*/RT}$$

where E_a^* is the activation energy for thermal ignition, A is the pre-exponential factor, and T is the absolute temperature. E_a^* was determined from the slope of a plot of $\ln(D_i)$ versus $1/T$. The percent oxygen balance (OB) was calculated by the following equation³⁹

$$OB = [(z - 2x - y/2)100]/n$$

where x , y , z are the number of atoms of C, H, N, respectively, and n is the total number of atoms in the molecule.

Kinetic Analysis of Isothermal TG Data. Kinetic analysis of solid state decomposition is usually based on a single step kinetic equation⁴⁰

$$d\alpha/dt = k(T)f(\alpha) \quad (1)$$

where t is the time, T is the temperature, α is the extent of conversion ($0 < \alpha < 1$), $k(T)$ is the rate constant, and $f(\alpha)$ is the reaction model,⁴¹ which describes the dependence of the reaction rate on the extent of reactions. The value of α is experimentally derived from the global mass loss in TG experiments. The reaction model may take various forms; the temperature dependence of $k(T)$ can be satisfactorily described by the Arrhenius equation, whose substitution into eq 1 yields

$$d\alpha/dt = A \exp(-E/RT)f(\alpha) \quad (2)$$

where A is pre-exponential factor, E is the activation energy, and R is the gas constant.

Model Fitting and Isoconversional Method. Rearrangement and integration of eq 1 for isothermal conditions give

$$g_j(\alpha) = k_j(T)t \quad (3)$$

where $g(\alpha) = \int_0^\alpha [f(\alpha)]^{-1} d\alpha$ is the integrated form of the reaction model. The subscript j has been introduced to emphasize that on substituting a particular reaction model in eq 3 results in evaluating the corresponding rate constant, which is determined from the slope of a plot for $g_j(\alpha)$ versus t . For each reaction model selected, the rate constants are evaluated at several temperatures T_i and Arrhenius parameters are determined using the Arrhenius eq 4 in its logarithmic form.

$$\ln k_j(T_i) = \ln A_j - E_j/RT_i \quad (4)$$

Arrhenius parameters were evaluated for isothermal experimental data by the model fitting method. The isoconversional method allows the evaluation of the activation energy without making any assumptions about the reaction model. In addition, this method evaluates the effective activation energy as a function for the extent of conversion which allows one to explore multistep kinetics. The basic assumption of this method⁴¹ is that the reaction model as defined in eq 1 is not dependent on temperature or heating rate. Under isothermal conditions, on combining eqs 3 and 4 we get

$$-\ln t_{\alpha,i} = \ln[A_\alpha/g(\alpha)] - E_\alpha/RT_i \quad (5)$$

where E_α could be evaluated from the slope of the plot of $-\ln t_{\alpha,i}$ against T_i^{-1} . Thus, E_α were calculated for 1–4 at various α_i .

3. RESULTS AND DISCUSSION

3.1. Infrared and NMR Spectroscopy. The asymmetric and the symmetric stretching vibrations of $-\text{NO}_2$ group show bands at 1536 and 1334 cm^{-1} , respectively.^{42,43} As compared to the free picric acid vibration (1607 cm^{-1}), the $\nu_{\text{as}}(\text{NO}_2)$ vibrations appear in the range 1581–1530 cm^{-1} in the complexes 1–4. The NH stretching vibration is normally observed at 3500–3400 cm^{-1} , which is shifted to lower wavenumber. The shifting toward lower frequency is due to the hydrogen bonded noncovalent interactions between donor ($-\text{NH}$ protons) and acceptor (picrate anion).^{44,45} The presence of hydrogen bond interactions in the solution (1–4) was confirmed by the prominent downfield chemical shift in the ^1H NMR spectra of each case with respect to the free ligand.

3.2. Structure Description of Complexes 1–4. Complex 1 is crystallized in the triclinic system with space group $P\bar{1}$. An asymmetric unit consists of one molecule of deprotonated PA, one molecule of protonated phen, and one methanol molecule. In 1, the acidic hydrogen of the hydroxyl group on picric acid was transferred to the one nitrogen atom of phen as shown in Figure 1.

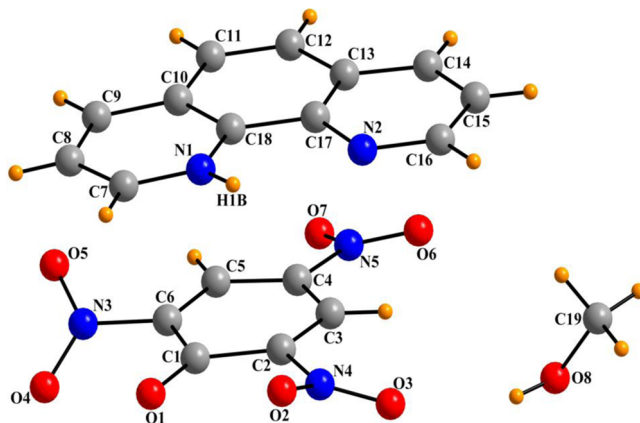


Figure 1. Molecular structure of 1. Color code: C, gray; H, orange; O, red; N, blue.

The protonated nitrogen (N1) shows the strong hydrogen bonding with the oxygen atom (O8) of methanol molecule via $\text{N1-H1B}\cdots\text{O8}$ [1.831(29) Å] interaction. The crystal packing also shows other $\text{C-H}\cdots\text{O}$ [C7–H7A \cdots O1, 2.338(18) Å; C7–H7A \cdots O2, 2.404(9) Å; C9–H9 \cdots O3, 3.016(19) Å; C11–H11 \cdots O3, 2.628(9) Å; C12–H12 \cdots O6, 2.840(21) Å; C14–H14 \cdots O7, 2.410(2) Å; C15–H15 \cdots O8, 2.839(5) Å; C16–H16 \cdots O8, 2.807(4) Å; C19–H19C \cdots O3, 2.746(3) Å] and $\text{O-H}\cdots\text{O}$ [O8–H8 \cdots O1, 2.002(3) Å; O8–H8 \cdots O4, 2.419(19) Å] noncovalent interactions as shown in Figure S1, Supporting Information. Stacking of both organic moieties with methanol molecules make three-dimensional ladder like structure, where the methanol molecules act as the pillars (Figure S2, Supporting Information).

The complex 2 with two molecules of anionic deprotonated PA and one molecule of cationic protonated terpy in asymmetric unit crystallizes in monoclinic crystal system with space group $P2_1/c$ as shown in Figure 2.

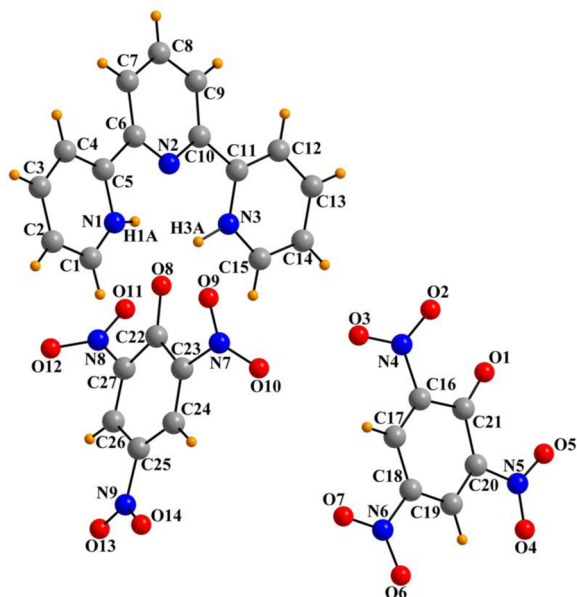


Figure 2. Molecular structure of **2**. Color code: C, gray; H, orange; O, red; N, blue.

The protonated nitrogen atoms (N1, N3) of terpy molecule present the strong hydrogen bonding with the oxygen atom (O8) of picrate anion via N–H...O [N1–H1A...O8, 2.031(110) Å; N3–H3A...O8, 1.727(49) Å] noncovalent interactions. The other intermolecular interactions C–H...O [C4–H4...O12, 2.697(3) Å; C7–H7...O11, 2.714(3) Å; C7–H7...O12, 2.619(3) Å; C8–H8...O5, 2.949(8) Å; C9–H9...O1, 2.287(5) Å; C12–H12...O1, 2.380(4) Å; C13–H13...O2, 2.489(8) Å; C13–H13...O11, 2.600(3) Å; C14–H14...O5, 2.121(7) Å; C15–H15...O4, 2.328(7) Å] and O...O [O13...O6, 2.968(6) Å; O14...O6, 3.010(5) Å] are also present (Figure S3, Supporting Information). Due to the presence of various noncovalent interactions, **2** shows three-dimensional spiral view (Figure S4, Supporting Information).

The asymmetric unit of the complex **3** contains one molecule of deprotonated PA and one molecule of protonated hmta as shown in Figure 3. It is crystallized in monoclinic with $P2_1/c$ space group.

This complex reveals different intermolecular interactions viz., C–H...O [C7–H7B...O5, 2.925(2) Å; C8–H8B...O4,

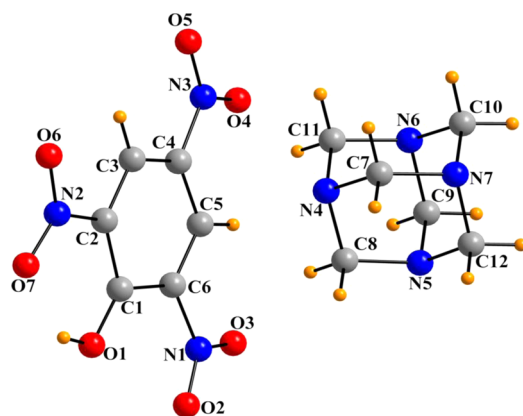


Figure 3. Molecular structure of **3**. Color code: C, gray; H, orange; O, red; N, blue.

2.804(4) Å; C9–H9B...O1, 2.987(1) Å; C9–H9B...O3, 2.918(2) Å; C9–H9B...O6, 2.707(1) Å; C9–H9B...O7, 3.017(2) Å; C11–H11B...O3, 2.590(2) Å; C12–H12A...O4, 2.401(1) Å; C–H...N [C7–H7A...N7, 2.800(2) Å; C8–H8A...N5, 2.852(1) Å; C8–H8B...N4, 2.817(1) Å; C8–H8B...N5, 3.074(2) Å; C10–H10B...N7, 2.801(3) Å; C11–H11B...N4, 2.724(2) Å; C12–H12A...N7, 3.071(1) Å; C12–H12B...N7, 2.908(3) Å] and N–H...O [N6–H6...O1, 1.864(25) Å] between cations and anions (Figure S5, Supporting Information). The crystal packing also shows that the C–H...N interactions play a key role in the self-assembly of the hmtaH⁺ to generate one-dimensional zigzag chain (i.e., CH₂ groups of one hexamine form C–H...N interactions with the nitrogen atoms of the neighboring hmtaH⁺), whereas on the other side PA[−] stacks one above the other molecule through the C–H...O [C3–H3...O2, 2.958(2) Å] interactions. All these noncovalent interactions are involved in an entirely different three-dimensional packing as alternate channels of picrates and protonated hmta, which are hydrogen bonded to one another (Figure S6(a), S6(b), Supporting Information).

The cocrystallization of picric acid with tptz resulted in the formation of complex **4**, crystallizes in triclinic system with space group $P\bar{1}$ and has one protonated tptz cation and three picrate anions, where only pyridyl nitrogen atoms (N10, N12, N15) are protonated by the proton of the hydroxyl group present on picric acid (Figure 4).

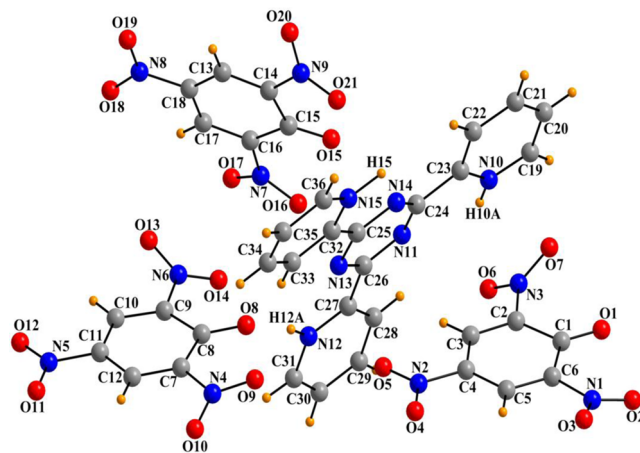


Figure 4. Molecular structure of **4**. Color code: C, gray; H, orange; O, red; N, blue.

As shown in Figure S7 (Supporting Information), seven molecules of picrate anion are interlinked with each other through the weak O...O [O3...O10, 3.308 Å; O3...O15, 3.558 Å; O5...O9, 3.570 Å; O10...O20, 3.475 Å; O13...O17, 3.536 Å; O14...O16, 3.105 Å] noncovalent interactions and are formed as a pseudocavity for the guest tptzH₃³⁺ molecule. The guest molecule resides in a cavity via N–H...O and C–H...O interactions. C–H and three protonated pyridyl N–H of tptz are involved in the C–H...O [C19–H19...O14, 2.484(5) Å; C19–H19...O17, 2.795(8) Å; C20–H20...O27, 2.633(5) Å; C21–H21...O18, 2.661(2) Å; C22–H22...O20, 2.839(8) Å; C28–H28...O15, 2.649(6) Å; C28–H28...O16, 2.534(6) Å; C29–H29...O15, 2.601(6) Å; C33–H33...O8, 1.955(4) Å] and N–H...O [N10–H10...O17, 2.637(24) Å; N12–H12...O8, 1.931(26) Å; N15–H15...O20, 2.243(29) Å; N15–H15...O21, 2.777(29) Å] interactions with the oxygen atom of picrate anions (Figure S8, Supporting Information). The presence of

different noncovalent interactions between picrates and protonated tptz causes the formation of entirely different packing views (Figure S9, Supporting Information).

3.3. DFT and Statistical Analysis. The optimized structural parameters of all individual N-heterocyclic bases, picric acid, and their complexes were calculated with B3LYP/6-31G** basis sets. Each optimized geometry showed positive vibrational frequencies and suggested that the optimized structure was the global minimum on the potential energy surface. The single point energy calculations were performed for recording the zero point corrected total energies of various species. In addition to the characterization of these complexes, the gas phase geometries, harmonic vibrational frequencies, and binding energies of these acid–base complexes were computed. The B3LYP predicted structures and geometrical parameters of 1–4 are given in Figure 5 and Table S1 (Supporting Information), respectively.

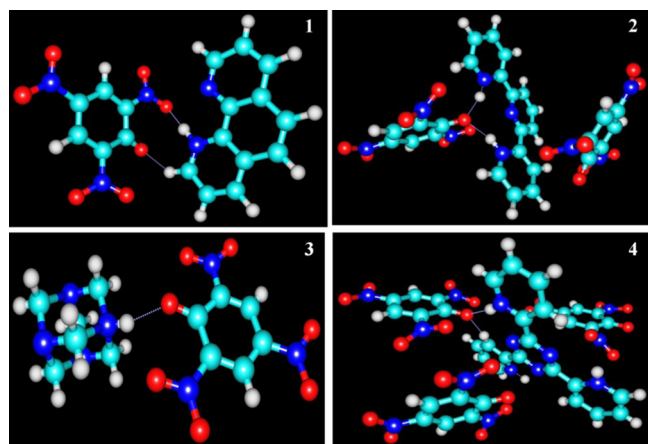


Figure 5. Optimized geometry of 1–4. Color code: C, cyan; H, white; O, red; N, blue.

The hydrogen bond interaction energies were determined according to the following equation

$$\Delta E = E_{\text{complex}} - (E_x + E_{\text{acid}})$$

where E_{complex} , E_x , and E_{acid} are the zero point corrected total energies of complexes, N-heterocyclic bases, and acid calculated at the B3LYP/6-31G** level of theory. We have removed the solvent molecules to check the relative stability. The trend observed for the hydrogen bond interaction energy is given in Table 3. DFT calculation shows that, as the nitrogen atom increases in the base, the hydrogen bond interaction energy increases.

There is a slight difference in hydrogen bond interaction energy in 1 and 2, as both have almost the same number of interactions, but in the case of 3, the energy is almost 2 times higher than that of 1 due to the double nitrogen atoms in

Table 3. Hydrogen Bond Interaction Energy (kcal/mol)

S no.	complexes	hydrogen bond interaction energy/ kcal mol ^{−1}
1	[PA [−] ·phenH ⁺ ·CH ₃ OH] (1)	09.46
2	[2PA [−] ·terpyH ₂ ²⁺] (2)	12.50
3	[PA [−] ·hmtaH ⁺] (3)	18.72
4	[3PA [−] ·tptzH ₃ ³⁺] (4)	21.49

hmtaH⁺. The hydrogen bond interaction energy is highest in 4 due to the presence of more acid molecules in the unit cell, which shows the higher contribution in the strong and weak hydrogen bond interactions with the protonated 2,4,6-tris(2-pyridyl)-1,3,5-triazine. The negligible difference in the energy (Table S2, Supporting Information) between the optimized structure and crystal structure of 1–4 suggests that the orientation and interaction remain almost the same in both the gas and the solid phase. From statistical analysis, it is found that the *p*-value is <0.05 in all above cases (structural parameters). From this, we can conclude that theoretical (DFT) values are statistically closed to actual experimental (XRD) values.

3.4. Thermal Analysis. The thermal stability of 1–4 is demonstrated by thermogravimetry (TG) and differential scanning calorimetry (DSC). The thermoanalytical data are listed in Table 4, and the TGA-DSC curves are shown in Figure

Table 4. TG-DSC Data of 1–4 under a N₂ Atmosphere

complexes	TG			DSC	
	T _i / °C	T _f / °C	α	peak temp/°C	nature
[PA [−] ·phenH ⁺ ·CH ₃ OH] (1)	104 155	129 281	7.1 95.3	133 241	endo exo
[2PA [−] ·terpyH ₂ ²⁺] (2)	190	307	97.9	294	exo
[PA [−] ·hmtaH ⁺] (3)	289	381	98.2	329	exo
[3PA [−] ·tptzH ₃ ³⁺] (4)	283	310	97.1	319	exo

6. The TG thermogram clearly indicates that thermal decomposition of 1 occurs in two steps. First weight loss (7.1%) occurs at around 129 °C due to the loss of methanol molecule. Beyond this temperature (155–281 °C), a plateau is observed, where 95.3% mass loss occurs due to the removal of both picrate and protonated phen. 2 decomposes immediately after melting, and the decomposition continues up to 307 °C with 97.9% weight loss due to the release of both cation and anion. The sharp exothermic peak for 2 is perceived at 294 °C. The thermal decomposition of 3 in the temperature range 289–381 °C shows the weight loss of 98.2% with the exothermic peak at 329 °C due to the release of both picrate and hmtaH⁺. The same behavior is also observed in 4; i.e., 97.1% weight loss occurs due to the thermal decomposition of cation and anion at 283–310 °C with exothermic peak at 319 °C. The sharp exothermic peak in 1–4 indicates a good degree of crystallinity.⁴⁶

The kinetics of thermal decomposition for 1–4 was evaluated using 14 mechanisms based kinetic models as given in Table S3, Supporting Information. The set of reaction models⁴⁰ was used to analyze the isothermal TG data in the range 290–330 °C for 1–4 (Figure 7), to calculate the E_a values for thermal decomposition, which were done in the range of decomposition/vaporization using an indigenously fabricated TG apparatus. The activation energy values are reported in Table 5.

In the model fitting method, the kinetics is analyzed by choosing a “best fit” model based on the value of the correlation coefficient *r* close to 1. Average values 37.2, 39.0, 42.3, and 78.7 kJ mol^{−1} have been obtained as activation energies for isothermal decomposition of 1–4. The isoconversional method is being used to establish a relation between the activation energy and the extent of conversion (α) of the sample. According to Figure 8, for a particular complex each

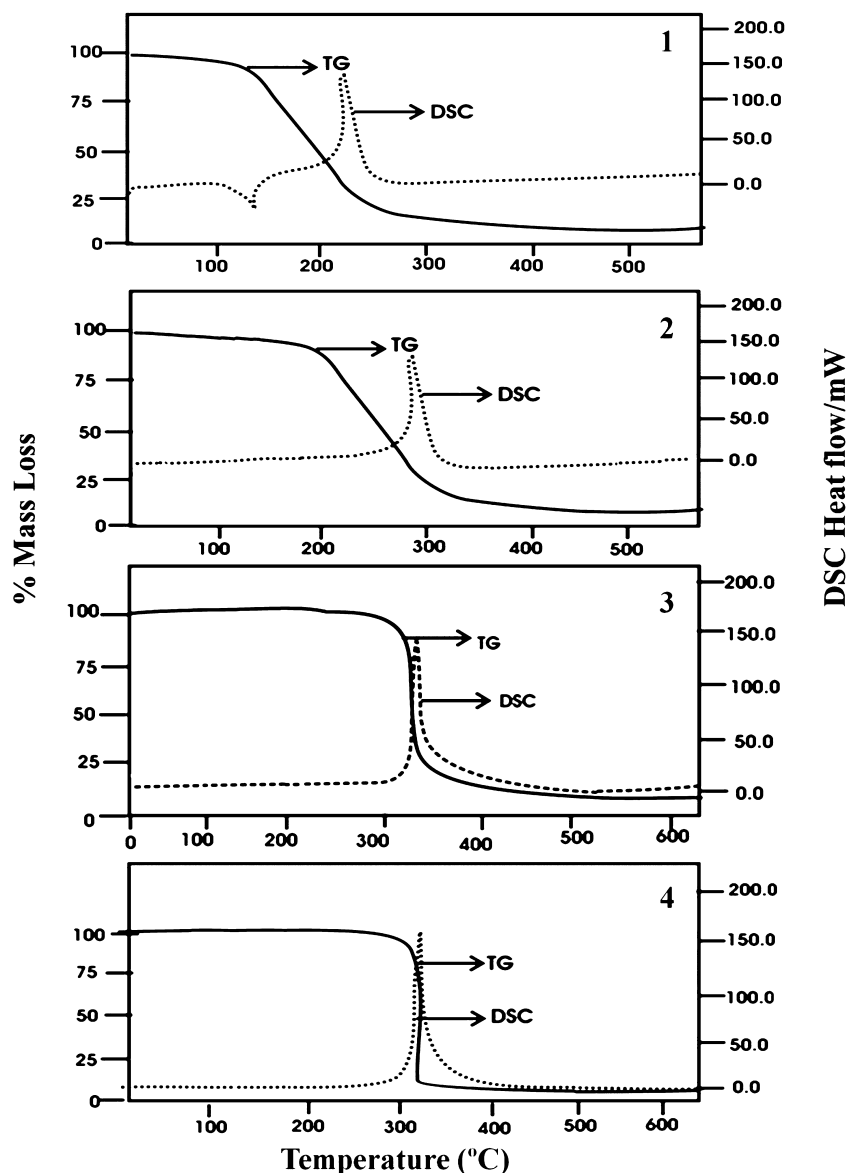


Figure 6. Simultaneous TG-DSC of 1–4 in a nitrogen atmosphere.

activation energy has a separate value at different α 's. Although these are stable at room temperature, they ignite when subjected to sudden high temperature.

Freeman and Gordon³⁸ have suggested the following heat balance equation to evaluate the preignition reactions

$$dQ_H/dt = dH/dt - dq/dt \quad (6)$$

where dQ_H/dt is the net rate of heat gain in the system, dH/dt is the rate of heat produced by preignition reactions, and dq/dt is the rate of heat dissipation.

Ignition will occur when

$$Q_H = H' \quad (7)$$

where H' is the minimum amount of heat required to raise the temperature of the system to the point of ignition. From eq 7, it follows that

$$Q_H = H - q \quad (8)$$

where H is the total heat produced by preignition reactions. The ignition would occur only if $H - q \geq H'$. The total heat

produced by the preignition reactions must be greater than H' by the amount of heat dissipated. Thus

$$H = H' + q \quad (9)$$

The following equation was derived by Freeman and Gordon.³⁸

$$t_{id} = Ae^{\Delta H^*/RT} \quad (10)$$

where ΔH^* is the heat of activation and is approximately equal to activation energy (E^*). If the activity of the reactants does not change significantly during preignition reactions, the log of the time of ignition should be a linear function of the reciprocal for the absolute temperature and the relation comes out to be as given in eq 10.

Further, to evaluate the sensitivity of these complexes, their ignition delay measurements were carried out in the temperature range 380–420 °C (Table 6). For 1–4, E_a^* was determined from the slope of a plot for $\ln(D_i)$ versus $1/T$ (Figure 9). The energy of activation for ignition is 79.6, 89.2, 99.9, and 108.3 kJ mol^{−1} for 1–4, respectively. The energy of activation for ignition (E^*) is in the order 4 > 3 > 2 > 1. The

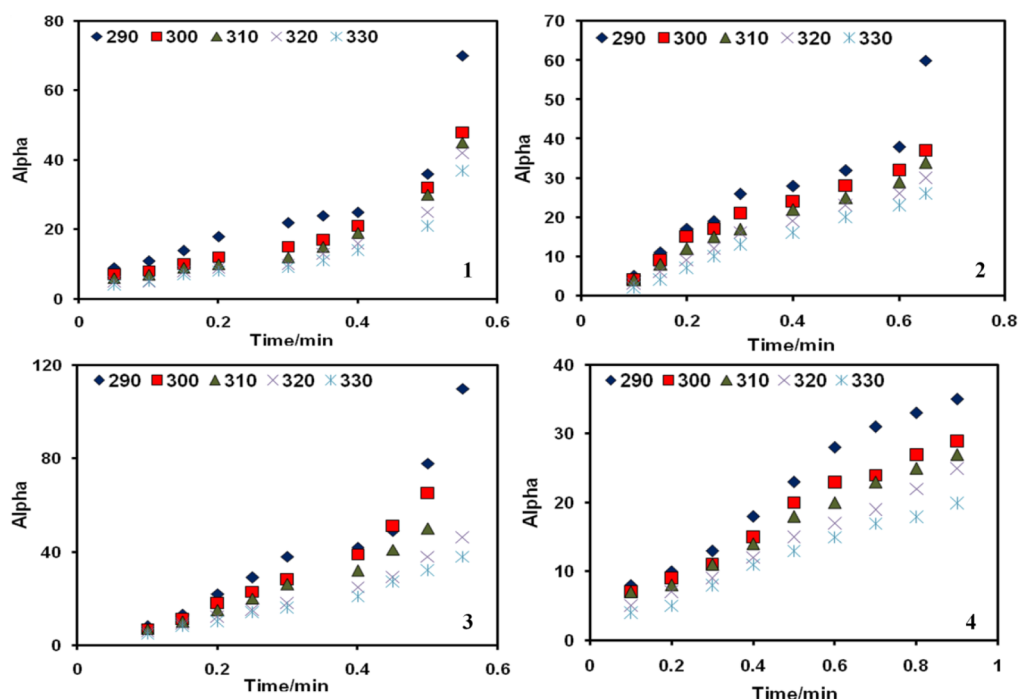
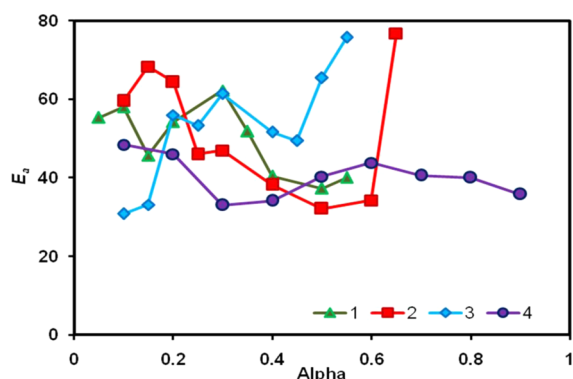


Figure 7. Isothermal TG of 1–4 in static air atmosphere.

Table 5. Arrhenius Parameters for Isothermal Decomposition for 1–4

model ^a	[PA [−] ·phenH ⁺ ·CH ₃ OH] (1)		[2PA [−] ·terpyH ₂ ²⁺] (2)		[PA [−] ·hmtaH ⁺] (3)		[3PA [−] ·tptzH ₃ ³⁺] (4)	
	E _a	r	E _a	r	E _a	r	E _a	r
1	35.4	0.899	38.2	0.980	45.6	0.896	81.7	0.997
2	35.5	0.900	38.1	0.980	45.6	0.897	81.6	0.997
3	35.7	0.900	38.2	0.980	45.4	0.900	81.4	0.997
4	36.7	0.907	38.1	0.983	44.1	0.914	80.0	0.997
5	37.0	0.911	38.2	0.984	43.2	0.919	79.3	0.997
6	36.6	0.908	39.0	0.985	43.5	0.915	79.9	0.997
7	36.0	0.902	38.4	0.983	45.3	0.912	80.7	0.997
8	35.8	0.902	38.5	0.983	44.9	0.903	81.1	0.997
9	36.0	0.903	38.6	0.984	44.6	0.906	80.8	0.997
10	37.3	0.907	38.6	0.985	44.0	0.912	80.1	0.997
11	36.5	0.902	39.7	0.951	41.8	0.905	78.6	0.998
12	36.4	0.906	38.4	0.984	44.2	0.911	80.3	0.997
13	35.5	0.901	38.7	0.983	45.1	0.922	81.4	0.997
14	37.2	0.915	39.0	0.985	42.3	0.923	78.7	0.997

^aEnumeration of the model is as given in Table S3, Supporting Information.Figure 8. Dependence of activation energy (E_a) on the extent of conversion (α) for 1–4.

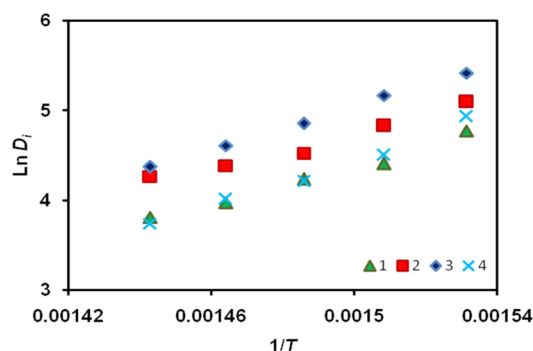
activation energies, calculated by isothermal TG and ignition delay measurements, have different values, which may be due to the different temperature ranges. The energy of ignition delay for 4 is highest compared to the others and may be due to stabilization of the molecules by a higher number of noncovalent interactions and a high hydrogen bond interaction energy. Being more stable, 4 has comparatively less tendency to decompose. The oxygen balance values indicate that these complexes are low explosives (Table 6).

4. CONCLUSIONS

In summary, structural characterization and thermal analysis of four newly synthesized supramolecular complexes containing picric acid and N-heterocyclic bases have been done experimentally as well as theoretically by using different physical techniques like elemental analysis, IR, NMR, single

Table 6. Ignition Delay Activation Energy for Thermal Ignition (E^*) and Correlation Coefficient (r)

complexes	D_i/s					$E^*/\text{kJ mol}^{-1}$	r	OB
	$380 \pm 1\text{ }^\circ\text{C}$	$390 \pm 1\text{ }^\circ\text{C}$	$400 \pm 1\text{ }^\circ\text{C}$	$410 \pm 1\text{ }^\circ\text{C}$	$420 \pm 1\text{ }^\circ\text{C}$			
$[\text{PA}^-\cdot\text{phenH}^+\cdot\text{CH}_3\text{OH}]$ (1)	163	125	92	80	71	79.6	0.984	−86.17
$[\text{2PA}^-\cdot\text{terpyH}_2^{2+}]$ (2)	118	82	69	53	45	89.2	0.992	−79.85
$[\text{PA}^-\cdot\text{hmtaH}^+]$ (3)	225	175	128	100	79	99.9	0.999	−59.75
$[\text{3PA}^-\cdot\text{tptzH}_3^{3+}]$ (4)	138	90	67	55	42	108.3	0.992	−72.58

Figure 9. Graph of $\ln D_i$ vs $1/T$.

crystal X-ray diffraction, and Gaussian 03 suite. The IR and NMR spectroscopic results of complexes 1–4 are in agreement with the result of X-ray crystallography, i.e., existence of hydrogen bonding between donor and acceptor. The structural analysis reveals that the three-dimensional structure of complexes 1–4 changes (ladder \rightarrow spiral \rightarrow channels \rightarrow host–guest) as noncovalent interaction increases when the number of nitrogen atoms in N-heterocyclic base increases. Other factors like type of interactions and orientation of the molecules in three-dimensional spaces are also responsible for the changes in the packing. The presence of a maximum number of noncovalent interactions in 4 may be responsible for the creation of a pseudocavity for trapping the tptzH_3^{3+} as a guest molecule. So we can say that the variation in the number of nitrogen atoms in N-heterocyclic bases plays a significant role in controlling the structure of these acid–base complexes. DFT studies showed that in both solid and gaseous phases, the structures of complexes 1–4 remain the same. The thermal stability of these complexes also increases as the nitrogen atoms increase in the bases. The results from the theoretical calculations and ignition delay measurements also suggested that the hydrogen bond interaction energy and activation energy of thermal ignition increases from complexes 1 to 4.

■ ASSOCIATED CONTENT

● Supporting Information

Additional figures of molecular arrangements and non-covalent interactions (Figures S1–S9) and tables of bond lengths and angles, solid phase and gas phase energies, and reaction models (Tables S1–S3). This information is available free of charge via the Internet at <http://pubs.acs.org>. CCDC numbers 867087–867090 contain the supplementary crystallographic data (CIF) for this article. These data can be obtained free of charge from the Director, CCDC, 12 Union Road, Cambridge CB2 1EZ, UK (Fax: +44–1223–336–033; e-mail deposit@ccdc.cam.ac.uk or <http://www.ccdc.cam.ac.uk>).

■ AUTHOR INFORMATION

Corresponding Author

*N. Goel: tel, +91-09412841504; e-mail, nidhigoel.iitr@gmail.com.

Notes

The authors declare no competing financial interest.

■ ACKNOWLEDGMENTS

Authors gratefully acknowledge Prof. Gurdip Singh and Dr. Pratibha Srivastava (Department of Chemistry, DDU Gorakhpur University, Gorakhpur, India) for giving us the possibility to use the facilities present in his research laboratory (ignition delay measurements) and for the fruitful discussions on the results and IITR for instrumental facilities.

■ REFERENCES

- (1) Zaworotko, M. J. Molecules to Crystals, Crystals to Molecules ... and Back Again? *Cryst. Growth Des.* **2007**, *7*, 4–9.
- (2) Childs, S. L.; Stahly, G. P.; Park, A. The Salt-Cocrystal Continuum: The Influence of Cocrystal Structure on Ionization State. *Mol. Pharm.* **2007**, *4*, 323–338.
- (3) Wuest, J. D. Engineering Crystals by the Strategy of Molecular Tectonics. *Chem. Commun.* **2005**, 5830–5837.
- (4) Lehn, J. M. From Supramolecular Chemistry Towards Constitutional Dynamic Chemistry and Adaptive Chemistry. *Chem. Soc. Rev.* **2007**, *36*, 151–160.
- (5) Boldog, I.; Dran, J. C.; Chernega, A. N.; Rusanov, E. B.; Krautscheid, H.; Domasevitch, K. V. Hydrogen Bonding Patterns and Supramolecular Structure of 4,4'-Bipyrazolium Salts. *Cryst. Growth Des.* **2009**, *9*, 2895–2905.
- (6) Burrows, A. D. Crystal Engineering Using Multiple Hydrogen Bonds. *Struct. Bonding (Berlin)* **2004**, *108*, 55–96.
- (7) Näntinen, K. I.; Rissanen, K. Dendritic Pyridine-Functionalized Polyesters and Their Polycationic Hydrogen Bonded Picrates: Synthesis and X-ray Structural Study of Weak Hydrogen Bonding. *Cryst. Growth Des.* **2003**, *3*, 339–353.
- (8) Steiner, T. The Hydrogen Bond in the Solid State. *Angew. Chem., Int. Ed.* **2002**, *41*, 48–76.
- (9) Steiner, T.; Saenger, W. Role of C–H...O Hydrogen Bonds in the Coordination of Water Molecules. Analysis of Neutron Diffraction Data. *J. Am. Chem. Soc.* **1993**, *115*, 4540–4547.
- (10) Thaimattam, R.; Xue, F.; Sarma, J. A. R. P.; Mak, T. C. W.; Desiraju, G. R. Inclusion Compounds of Tetrakis(4-nitrophenyl)-methane: C–H...O Networks, Pseudopolymorphism, and Structural Transformations. *J. Am. Chem. Soc.* **2001**, *123*, 4432–4445.
- (11) Perlstein, J. *The Weak Hydrogen Bond In Structural Chemistry and Biology* (International Union of Crystallography, Monographs on Crystallography, 9). By Gautam R. Desiraju (University of Hyderabad) and Thomas Steiner (Freie Universität Berlin). Oxford University Press: Oxford and New York, 1999. xiv + 507 pp. \$150. ISBN 0-19-850252-4. *J. Am. Chem. Soc.* **2001**, *123*, 191–192.
- (12) Desiraju, G. R.; Steiner, T. *The Weak Hydrogen Bond in Structural Chemistry and Biology*; Oxford University Press: Oxford, U.K., 1999.
- (13) Friscic, T.; Trask, A. V.; Motherwell, W. D. S.; Jones, W. Guest-Directed Assembly of Caffeine and Succinic Acid into Topologically

Different Heteromolecular Host Networks upon Grinding. *Cryst. Growth Des.* **2008**, *8*, 1605–1609.

(14) Takata, N.; Shiraki, K.; Takano, R.; Hayashi, Y.; Terada, K. Cocystal Screening of Stanolone and Mestanolone Using Slurry Crystallization. *Cryst. Growth Des.* **2008**, *8*, 3032–3037.

(15) Srinivasan, P.; Kanagasekaran, T.; Gopalakrishnan, R.; Bhagavannarayana, G.; Ramasamy, P. Studies on the Growth and Characterization of L-Asparaginium Picrate (LASP): A Novel Non-linear Optical Crystal. *Cryst. Growth Des.* **2006**, *6*, 1663–1670.

(16) Yamaguchi, S.; Goto, M.; Takayanagi, H.; Ogura, H. The Crystal Structure of Phenanthrene: Picric Acid Molecular Complex. *Bull. Chem. Soc. Jpn.* **1988**, *61*, 1026–1028.

(17) In, Y.; Nagata, H.; Doi, M.; Ishida, T.; Wakahara, A. Imidazole-4-acetic Acid-Picric Acid (1/1) Complex. *Acta Crystallogr.* **1997**, *C 53*, 367–369.

(18) Bertolasi, V.; Gilli, P.; Gilli, G. Hydrogen Bonding and Electron Donor–Acceptor (EDA) Interactions Controlling the Crystal Packing of Picric Acid and Its Adducts with Nitrogen Bases. Their Rationalization in Terms of the pK_a Equalization and Electron-Pair Saturation Concepts. *Cryst. Growth Des.* **2011**, *11*, 2724–2735.

(19) Dobrowolska, W. S.; Bator, G.; Sobczyk, L.; Grech, E.; Scheibe, J. N.; Pawlukojc, A.; Wuttke, J. The (2:1) Complex of Picric Acid with Tetramethylpyrazine: The Structure, IR Spectra and Tunnel Splitting of Methyl Groups. *J. Mol. Struct.* **2010**, *975*, 298–302.

(20) Srinivasan, P.; Kanagasekaran, T.; Gopalakrishnan, R. A. Highly Efficient Organic Nonlinear Optical Donor–Acceptor Single Crystal: L-Valinium Picrate. *Cryst. Growth Des.* **2008**, *8*, 2340–2345.

(21) Yathirajan, H. S.; Narayana, B.; Swamy, M. T.; Sarojini, B. K.; Bolte, M. Phthalazin-1(2H)-one-Picric Acid (1/1). *Acta Crystallogr.* **2008**, *E 64*, o119–o119.

(22) Singh, R. P.; Verma, R. D.; Meshri, D. T.; Shreeve, J. M. Energetic Nitrogen-Rich Salts and Ionic Liquids. *Angew. Chem., Int. Ed.* **2006**, *45*, 3584–3601.

(23) Llamas-Saiz, A. L.; Foces-Foces, C.; Echevarría, A.; Elguero, J. The Relative Basicities of Tris(pyrazol-1-yl)-1,3,5-triazine (TPT), Water and the Picrate Anion in the Solid State. *Acta Crystallogr.* **1995**, *C 51*, 1401–1404.

(24) Goel, N.; Singh, U. P.; Singh, G.; Srivastava, P. Study of Picrate Salts with Amines. *J. Mol. Struct.* **2013**, *1036*, 427–438.

(25) Singh, U. P.; Goel, N.; Singh, G.; Srivastava, P. Supramolecular Architecture of Picric Acid and Pyrazoles: Syntheses, Structural, Computational and Thermal Studies. *Supramol. Chem.* **2012**, *24*, 285–297.

(26) Sheldrick, G. M. *SADABS. Program for Empirical Absorption Correction of Area Detector Data*; University of Göttingen: Göttingen, Germany, 1996.

(27) Sheldrick, G. M. Phase Annealing in SHELX-90. Direct Methods for Larger Structures. *Acta Crystallogr.* **1990**, *A46*, 467–473.

(28) Sheldrick, G. M. *SHELXTL-NT Version 6.12, Reference Manual*; University of Göttingen: Göttingen, Germany, 2000.

(29) Brandenburg, K. *DIAMOND. Visual Crystal Structure Information System*, Version 2.1c; Crystal Impact GbR: Bonn, Germany, 2000.

(30) MERCURY, Cambridge Crystallographic Data Centre, 12 Union Road, Cambridge CB2 1EZ, U.K. Available from website: <http://www.ccdc.cam.ac.uk/>.

(31) *Gaussian 03*, Rev. C.02; Gaussian, Inc.: Wallingford, CT, 2004.

(32) Hariharan, P. C.; Pople, J. A. The Influence of Polarization Functions on Molecular Orbital Hybridization Energies. *Theo. Chem. Acta* **1972**, *28*, 213–222.

(33) Frisch, A.; Nielsen, A. B.; Holder, A. J. *GaussView Users Manual*; Gaussian Inc.: Wallingford, CT, 2003.

(34) Singh, G.; Singh, R. R. Indigenously Fabricated Apparatus for Thermogravimetric Analysis. *Res. Ind.* **1978**, *23*, 92–93.

(35) Singh, G.; Vasudeva, S. K.; Kapoor, I. P. S. Thermolysis of AP-PS-Additive Mixture II. *Indian J. Technol.* **1991**, *29*, 589–594.

(36) Zinn, J.; Rogers, R. N. Thermal Initiation of Explosives. *J. Phys. Chem.* **1962**, *66*, 2646–2653.

(37) Semenov, N. *Chemical Kinetics. Chain Reactions*; Clarendon Press: Oxford, U.K., 1935; Chapter 18.

(38) Freeman, E. S.; Gorden, S. The Application of the Absolute Rate Theory of the Nitrate–Magnesium, Sodium Nitrate–Magnesium. *J. Phys. Chem.* **1956**, *60*, 867–871.

(39) Martin, A. R.; Yallop, H. J. Some Aspects of Detonation of Part 1: Detonation Velocity and Chemical Constitution. *Trans Faraday Soc.* **1958**, *54*, 257–263.

(40) Brown, M. E.; Dollimore, D.; Galway, A. K. *Reaction in the Solid State. In Comprehensive Chemical Kinetics*; Elsevier: Amsterdam, The Netherlands, 1997; Vol. 22, pp 1–340.

(41) Singh, G.; Felix, P. S.; Pandey, D. K. Studies on Energetic Compounds Part 37: Kinetics of Thermal Decomposition of Perchlorate Complexes of Some Transition Metals with Ethylenediamine. *Thermochim. Acta* **2004**, *411*, 61–71.

(42) Singh, R. P.; Gao, H.; Meshri, D. T.; Shreeve, J. M. Nitrogen Rich Heterocycles. *Struct. Bonding (Berlin)* **2007**, *125*, 35–83.

(43) Ghazaryan, V. V.; Fleck, M.; Petrosyan, A. M. Glycine Glycinium Picrate-Reinvestigation of the Structure and Vibrational Spectra. *Spectrochim. Acta* **2011**, *A78*, 128–132.

(44) Ikeda, C.; Nagahara, N.; Motegi, E.; Yoshioka, N.; Inoue, H. Self-assembly of Monopyrazolporphyrins by Hydrogen Bonding in Solution. *Chem. Commun.* **1999**, *43*, 1759–1760.

(45) Silverstein, R. M.; Bassler, G. C.; Morrill, T. C. *Spectrometric Identification of Organic Compounds*, 5th ed.; John Wiley: New York, 1991.

(46) Chandramohan, A.; Bharathikannan, R.; Kandhaswamy, M. A.; Chandrasekaran, J. Synthesis, Crystal Growth, Spectral, Thermal and Optical Properties of Acenaphthene Picrate. *Cryst. Res. Technol.* **2008**, *43*, 93–98.